remote sensing

MDPI

Article

Radar-Derived Internal Structure and Basal Roughness Characterization along a Traverse from Zhongshan Station to Dome A, East Antarctica

Kun Luo [1,2], Sixin Liu [1], Jingxue Guo [2], Tiantian Wang [3], Lin Li [2], Xiangbin Cui [2], Bo Sun [2] and Xueyuan Tang [2,*]

1 College of Geo-Exploration Science and Technology, Jilin University, Changchun 130026, China; luokun17@mails.jlu.edu.cn (K.L.); liusixin@jlu.edu.cn (S.L.)
2 State Oceanic Administration Key Laboratory for Polar Science, Polar Research Institute of China, Shanghai 200136, China; guojingxue@pric.org.cn (J.G.); lilin@pric.org.cn (L.L.); cuixiangbin@pric.org.cn (X.C.); sunbo@pric.org.cn (B.S.)
3 Department of Survey Science and Engineering, College of Information Science and Engineering, Shandong Agricultural University, Taian 271018, China; wtt@sdau.edu.cn
* Correspondence: tangxueyuan@pric.org.cn

Received: 19 February 2020; Accepted: 25 March 2020; Published: 27 March 2020

Abstract: The internal layers of ice sheets from ice-penetrating radar (IPR) investigation preserve critical information about the ice-flow field and englacial conditions. This paper presents a new detailed analysis of spatial distribution characteristics of internal layers and subglacial topography of the East Antarctic ice sheet (EAIS) from Zhongshan Station to Dome A. The radar data of 1244 km along a traverse between Zhongshan Station and Dome A of EAIS were collected during the 29th Chinese National Antarctic Research Expedition (CHINARE 29, 2012/2013). In this study, the Internal Layering Continuity Index (ILCI) and basal roughness were taken as indicators to provide an opportunity to evaluate the past internal environment and dynamics of the ice sheet. Except for the upstream of Lambert Glacier, the fold patterns of internal layers are basically similar to that of the bed topography. The relatively flat basal topography and the decrease of ILCI with increasing depth provide evidence for identifying previous rapid ice flow areas that are unavailable to satellites, especially in the upstream of Lambert Glacier. Continuous internal layers of Dome A, recording the spatial change of past ice accumulation and ice-flow history over 160 ka, almost extend to the bed, with high ILCI and high basal roughness of the corresponding bed topography. There are three kinds of basal roughness patterns along the traverse, that is, "low ξ_t low η", "low ξ_t high η", and "high ξ_t high η", where ξ_t represents the amplitude of the undulations, and quantifies the vertical variation of the bedrock, and η measures the frequency variation of fluctuations and the horizontal irregularity of the profile. The characteristics of internal layers and basal topography of the traverse between Zhongshan Station and Dome A provide new information for understanding the ancient ice-flow activity and the historical evolution of EAIS.

Keywords: ice-penetrating radar (IPR); East Antarctica; internal layering continuity index (ILCI); roughness; ice dynamics

1. Introduction

The East Antarctic ice sheet (EAIS) is the world's largest ice body, and any minor change may cause global sea-level changes. The latest research shows that if climate change maintains its current rate, Totten Glacier, one of the most significant glaciers in East Antarctica, will retreat irreversibly and rapidly in the next century. This means that EAIS may be much more vulnerable than expected

by climate warming, and that its contribution to future global sea-level predictions may also be underestimated [1,2]. However, the lack of understanding of the structure and long-term evolution of EAIS limits the assessment of its potential changes. To achieve this goal, it is an effective way to quantify the characteristics of internal structure and basal topography of the ice sheet detected by ice radar [3].

Ice-penetrating radar (IPR) or radio-echo sounding (RES) systems operate by emitting electromagnetic waves into the air and the ice sheet, and the wave will be reflected at boundaries of different dielectric parameters [3]. The return signal records the ice thickness, internal layering, and basal conditions. Among them, the internal stratigraphy that can be traced over a long distance represents the same age layers (isochrones). Therefore, radar observations can provide not only information about the ice age [4,5], ice rheology [6–8], and ice conditions [9–11], but also constraints and tests for ice-sheet models [12–14], all of which play an irreplaceable role in the assessment of ice sheet mass balance and ice dynamics [15].

A layered structure is formed in the way that internal layers of the ice sheet are initially shaped by the surface accumulation and later modified by subsequent burial, compaction, and ice flow. Usually, the geometry of internal layers is affected by changes in substrate topography, basal conditions or accumulation rates, and ice flow effects [16,17]. Previous scholars used internal layers to study the relationship between the internal structure of the ice sheet and ice flow velocity [6,8,18]. There are two types of internal layers: one is a continuous and well-defined internal layer, which primarily follows surface and/or bed topography; another is a discontinuous internal layer that is buckled or disrupted layering. The discontinuous layering may be importantly affected by previous or current ice flow at different velocities [17,19]. Ice flow is also strongly dependent on bed conditions (thawed or frozen) and ice rheology [20–24]. Basal roughness is a significant indicator of bed conditions to infer ice dynamics and subglacial geomorphology interpretation [25,26]. It reflects the changing ice dynamics and thermal regimes with a historically superimposed ice sheet, which in turn modify the preglacial topography, underlying lithology, and geological structure [9,11,27]. The combination of ice velocity with internal layers and bed topography to study the ice sheet stability and ice dynamics has been widely used, including Greenland [3,28], the Institute and Möller Ice Streams [16,17], Pine Island Glacier [11,19,29], the Siple Coast ice streams in West Antarctica and the Wilkes Land, Wilkes Subglacial Basin, Aurora Subglacial Basin region [27,30], and Dronning Maud Land [31] in East Antarctica. Yet specific research is still lacking on the distribution characteristics of the internal layers of Princess Elizabeth Land (PEL) in East Antarctica.

As an important transect of the ITASE (International Trans-Antarctic Scientific Expedition) project, the inland traverse from the coastal Zhongshan Station to Dome A in East Antarctica has been continuously monitored by the CHINARE (Chinese National Antarctic Research Expedition) for 20 years. The traverse, passing through the western side of PEL, eastern upstream of Lambert Glacier, Gamburtsev Subglacial Mountains (GSM), and Dome A region, is shown in Figure 1 [32,33]. Ice thickness, subglacial topography, and internal layers were measured by IPR surveys [15,34,35]. Surface mass balance (SMB)/snow accumulation was measured by stake measurements and atmosphere was observed with automatic weather stations (AWS) [36,37]; surface topography and velocity were measured by the Global Positioning System (GPS) [38,39], which provide a reliable dataset to analyze age stratigraphy, ice dynamics, and mass balance of the ice sheet.

This paper gives a new detailed analysis and interpretation of internal layers and subglacial bed topography of EAIS from Zhongshan Station to Dome A. The vehicle-based deep IPR data were collected during the 29th Chinese National Antarctic Research Expedition CHINARE 29 (2012/2013). The Internal Layering Continuity Index (ILCI) and basal roughness index were used to quantitatively analyze the internal structure of radar profile and bed topography for preliminary interpretation and evaluation of ice flow behaviors and ice dynamics.

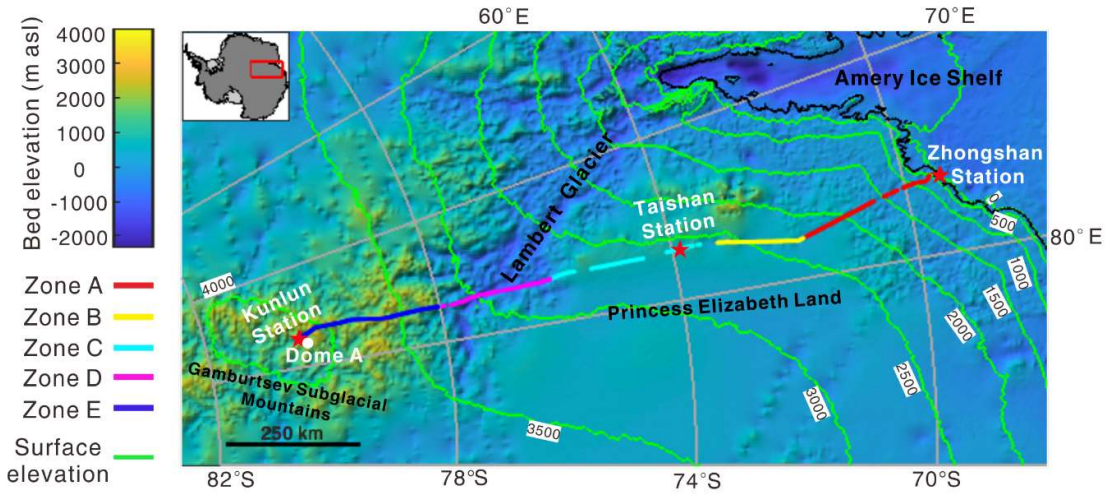

Figure 1. Map of the transect from Zhongshan to Dome A, East Antarctica. All of the bed elevation (the background image), surface elevation (the green line), and grounding line (the black line) are from Bedmap2 [40,41]. The red stars represent the locations of Zhongshan Station, Taishan Station, and Kunlun Station, respectively. The white point marks the location of Dome A.

2. Materials and Methods

2.1. IPR Data

In order to accurately measure the ice thickness, high-resolution internal structure, and subglacial topography, vehicle-based deep IPR was used along the 1244 km traverse (Figure 1) from Zhongshan (76.281 °E, 69.574 °S) to Dome A (77.133 °E, 80.409 °S) in EAIS during the CHINARE 29 (2012/2013). Zhongshan here refers to the starting point of the surveying line, 22.7 km away from the Zhongshan Station. The IPR, also called High-Resolution Ice-Sounding Radar (HRISR), is designed by the Institute of Electronics, Chinese Academy of Science to operate as a linear frequency modulated (LFM) pulse system with a center frequency of 150 MHz and a bandwidth of 100 MHz. The antenna system has two log-periodic antennas on a specialized versatile mobile observation cabin (SVMOC), which is 2 m above the snow surface (Figure 2). The main technical parameters of deep IPR are given in Table 1. The data acquisition system digitizes the return signal by a 12-bit analog-to-digital (A/D) converter at a sampling frequency of 500 MHz, and simultaneously records the GPS signal, fixed at horizontal error (< 7 m) and vertical error (< 10 m) [15].

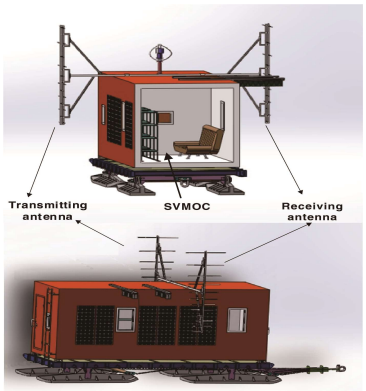

Figure 2. The position of log-periodic antennas on the snow vehicle. IPR hardware system mounted in the specialized versatile mobile observation cabin (SVMOC).

Table 1. The main technical parameters of deep ice-penetrating radar (IPR). The abbreviation of RF is repetition frequency (RF).

Parameter Name	Value	Units
RF carrier frequency	150	MHz
RF bandwidth	100	MHz
Rang sampling rate	500	MHz
Peak transmit power	500	W
Pulse repetition frequency	8000	Hz
Transmitted pulse duration	8	μs
Subglacial distance resolution	1.0	m
Polar ice detection depth	>3000	m

IPR data can be simply processed to get a clearer radar profile. Firstly, the first 2000 samples of the raw data are eliminated as they are included in the blind area caused by the receiver-blanking switcher for avoiding receiver saturation. Secondly, pulse compression [42,43] and coherent stack of 60 traces are carried out. Then, both the processing of direct current (DC) filters and mean filters processing are performed to reduce blurring noise [44]. Finally, conversion of time to depth is achieved by $h=v*t/2$, where v is the electromagnetic wave velocity in the ice sheet, and t is the time delay between the air-ice interface and the target. Here, a velocity equal to 0.168 m ns^{-1} was chosen to generate an ice thickness error of less than 20 m [15,45]. In the field, the failure to conduct an ice radar detection before the snowmobile in trouble-free operation made the acquired radar data geographically discontinuous. Matching each trace of the radar data with the GPS latitude and longitude recorded at the same time, the calculated gap of radar trace was 4 m with a relative error of 5 cm. The geographic location of the radar line was obtained as shown in Figure 1.

Based on the surface and subglacial characteristics, the transect from Zhongshan to Dome A can be divided into five zones for IPR profile analysis (Figure 3; Table 2). Zone A (0.0–262.0 km away from Zhongshan) has rapidly rising surface elevation with an average slope along the transect of 6.3 m km^{-1}. Zone B (267.2–431.7 km) is a slightly rising area with an average slope of 1.8 m km^{-1}. Zone C (461.7–752.1 km) is a relatively flat area with an average slope of 0.76 m km^{-1}. Zone D (752.1–972.2 km) is an upstream area of the Lambert Glacier and Zone E (972.2–1,243.7 km) is the Dome A region. The specific location of the radar line is shown in Table 2, and it is also marked with different colors in Figure 1.

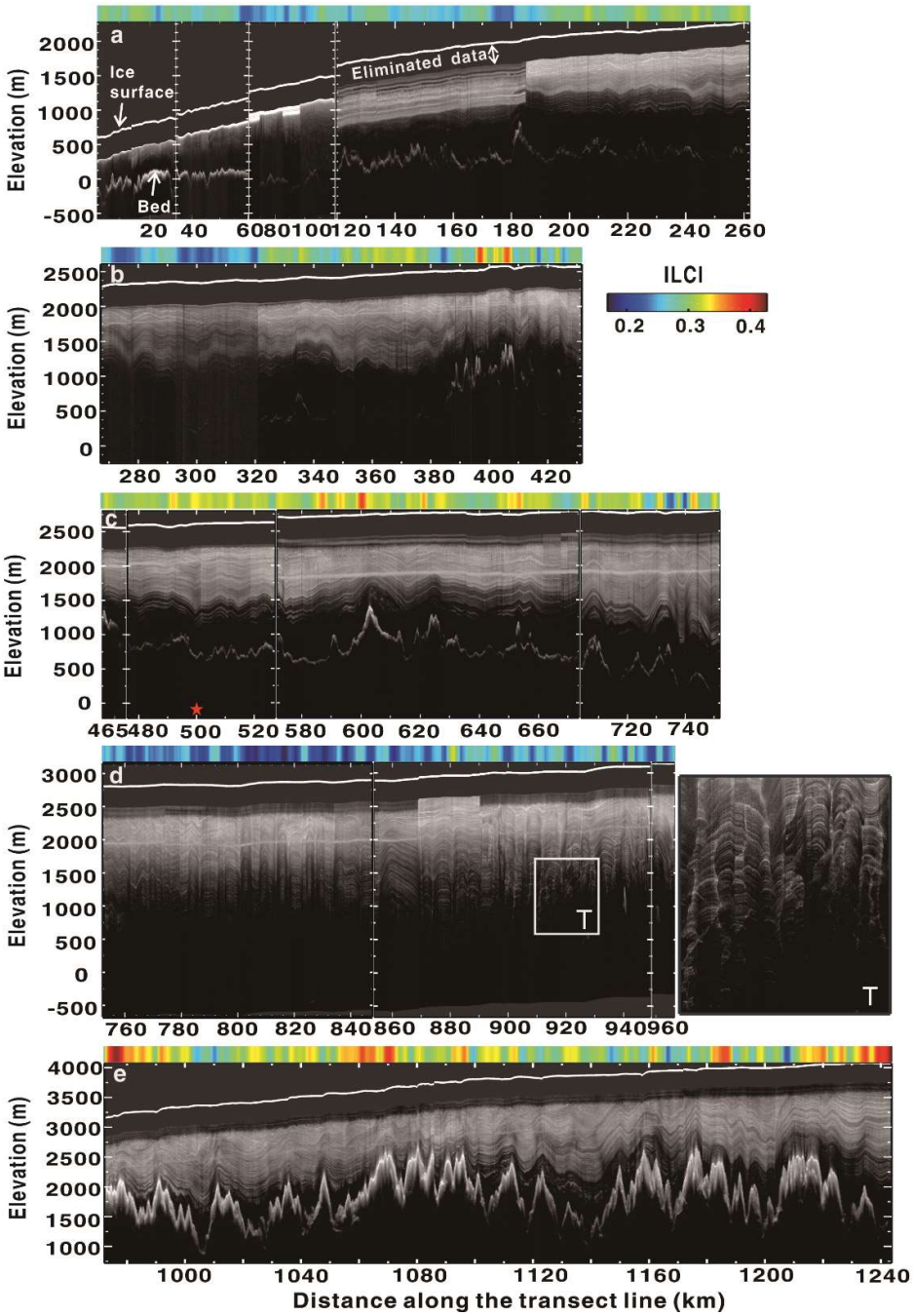

Figure 3. Radar profiles and Internal Layering Continuity Index (ILCI) diagram of the traverse from Zhongshan to Dome A. (**a**–**e**) represent the regions of Zone A, Zone B, Zone C, Zone D, and Zone E, respectively. ILCI is the result of the average from the 500-trace window. The red star marks the location of Taishan Station. The profile in T is the position of the white rectangle in Figure 3d. The white line in the radar profile indicates the surface, and the ice thickness of about 340 m (2000 sampling points) in the middle is the eliminated data.

Table 2. Location of each IPR line along the transect from Zhongshan to Dome A, East Antarctica. The abbreviations of Lat. and Long. are latitude and longitude, respectively.

Zone	Average Slope (m/km)	Start Distance (km)	End Distance (km)	Start Coordinate (Lat.(S), Long.(E))	End Coordinate (Lat.(S), Long.(E))
Zone A	6.28	0	12.835	(−69.574°,76.281°)	(−69.630°,76.464°)
		15.489	28.519	(−69.652°,76.490°)	(−69.765°,76.482°)
		34.355	34.766	(−69.817°,76.471°)	(−69.820°,76.468°)
		35.204	60.164	(−69.824°,76.468°)	(−70.041°,76.551°)
		71.289	74.454	(−70.140°,76.600°)	(−70.167°,76.620°)
		74.934	86.272	(−70.171°,76.622°)	(−70.270°,76.682°)
		90.091	100.008	(−70.303°,76.703°)	(−70.390°,76.751°)
		119.722	262.007	(−70.564°,76.856°)	(−71.783°,77.854°)
Zone B	1.80	267.158	431.655	(−71.827°,77.896°)	(−73.254°,77.095°)
Zone C	0.76	461.691	465.776	(−73.521°,76.978°)	(−73.557°,76.969°)
		467.071	467.947	(−73.569°,76.967°)	(−73.577°,76.966°)
		476.049	500.239	(−73.649°,76.964°)	(−73.864°,76.976°)
		502.719	502.811	(−73.886°,76.986°)	(−73.887°,76.986°)
		503.239	527.251	(−73.891°,76.987°)	(−74.105°,76.999°)
		571.584	664.503	(−74.502°,77.034°)	(−75.319°,76.912°)
		668.027	673.636	(−75.351°,76.919°)	(−75.398°,76.915°)
		703.885	752.080	(−75.669°,76.855°)	(−76.091°,76.974°)
Zone D	1.50	752.084	766.352	(−76.091°,76.974°)	(−76.218°,77.016°)
		766.800	784.441	(−76.222°,77.016°)	(−76.379°,77.029°)
		785.150	847.706	(−76.385°,77.028°)	(−76.943°,77.002°)
		853.704	853.836	(−76.997°,76.994°)	(−76.998°,76.993°)
		854.386	888.968	(−77.003°,76.993°)	(−77.310°,76.930°)
		890.802	890.902	(−77.327°,76.927°)	(−77.328°,76.926°)
		893.986	949.358	(−77.355°,76.916°)	(−77.829°,77.183°)
		958.895	965.183	(−77.914°,77.125°)	(−77.970°,77.120°)
		971.687	972.215	(−78.028°,77.104°)	(−78.032°,77.107°)
Zone E	3.35	972.219	972.223	(−78.032°,77.107°)	(−78.032°,77.107°)
		972.695	976.355	(−78.036°,77.101°)	(−78.068°,77.076°)
		976.881	977.201	(−78.073°,77.076°)	(−78.076°,77.075°)
		978.067	1087.2	(−78.083°,77.074°)	(−79.053°,76.939°)
		1089.600	1243.697	(−79.074°,76.912°)	(−80.409°,77.133°)

2.2. Internal Layer Continuity Index

The internal layer not only records the stratigraphic history of the ice sheet, but also holds the key information about the ideal state of ice and snow fallouts changed by daily wind, ice flow, and base melting. Continuous internal layers indicate that such processes that can reduce the number and strength of internal layers or reduce the returned radar power are weak or absent [10]. Previously, internal layers had been used to explain the relationship between the ice sheet's internal structure and ice-flow velocity in a qualitative manner [6,8,18]. Recently, the continuity index (CI) method proposed by Karlsson et al. [19] has been used to quantitatively characterize the apparently continuous and fractured internal layer regions from large-volume IPR datasets, which has been widely applied to assess the ice-flow history and ice dynamics [3,10,16,19,46].

Internal Layering Continuity Index (ILCI) is a calculated value of each A-scope that increases with the number and strength of the internal layer detected. It means that the gradient in each A-scope

trace can be used to quantify the continuity of internal layers based on the rapidity of signal variation between extremely low and high values [19], and detected spatial changes can be easily identified because of discontinuities in the number or strength of the internal layer [10]. Specifically, the mean absolute value of the derivative of reflected relative power is calculated in a time window sub-interval [L_1: L_2] between the ice surface and the basal interface, i.e.,

$$\Psi = \frac{1}{2\Delta r N} \sum_{i=L_1}^{L_2} \left| P_{i+1} - P_{i-1} \right| \quad (1)$$

where P_i is the reflected relative power (dB) at each time sample i and Δr is the depth (m). Given that M is the total number of time samples between the surface and substrate, a sub-interval N can be chosen as [(*1+M/5*): (*M-M/5*)] = [L_1: L_2], according to previous sensitivity experiments by Karlsson et al. [19] and Bingham et al. [16]. The upper and lower parts of the ice may be omitted to remove noise owing to the fact that the density differences of the upper ice cannot be well resolved by the chirped radar system and the lower ice often contains little or no internal layering [16,19]. The middle three-fifths of the ice column can be used to analyze and average over windows containing 500 traces (2 km) to assess overall layer continuity along the traverse. In essence, a high continuity index corresponds to clear internal layers, while sections with discontinuous or absent layers return a relative low continuity index [19].

2.3. Basal Roughness

Generally, basal roughness is defined as the degree of the vertical variation of topography within a given horizontal distance, which can be used to quantitatively describe the irregularity in a basal interface [26,47]. It has been applied to research on ice dynamics and subglacial geomorphological interpretation that the basal roughness of ice sheet acts as an indicator of subglacial conditions and a potential control of ice flow [11,25,27,30]. In most of the recent glaciological studies, a single-parameter roughness is defined as the integral of spectrum within a specified wavelength range, according to Fast Fourier Transform (FFT) analysis of bed topography [21,27,47]. As total roughness (ξ_t), this parameter represents the amplitude of undulations and is used to quantify the vertical variation of the bedrock, whereas resulting in the loss of information about the horizontal frequency [11]. Li et al. introduced a second parameter as frequency roughness (η) to explore the frequency variation of fluctuations. This measure is calculated as the total roughness index (ξ_t) divided by the bed slope index (ξ_{sl}). The parameter (η) corresponds to the horizontal irregularity of the section and invariant of the vertical stretching of the profile [25].

Here, the same method of a two-parameter roughness index (ξ_t and η) was used to quantitatively describe the basal roughness of both vertical and horizontal irregularities in the subglacial basal interface. First, the section of length (l) was chosen calculate the basal roughness. The length (l) is a moving window with 2^N sampling points, where N = 5 (32 sampling points = 128 m) as the suggested minimum value [47]. To explore the smallest possible scale of roughness patterns, a meter-scale range was also set for the length of the moving window [21,47]. Second, the spectral power density *S(k)* is calculated by FFT on the bed elevation (*Z(x)*) of which the mean bed elevation (<*Z(x)*>) is subtracted. The total roughness (ξ_t), indicating the amplitude of the elevation fluctuation, can be obtained by integrating *S(k)*.

$$\xi_t = \int_{k_1}^{k_2} S(k)dk = \int_{k_1}^{k_2} \left(\frac{1}{l} \int_{-\infty}^{\infty} Z_0(x) e^{-ikx} dx \int_{-\infty}^{\infty} Z_0(x') e^{-ikx'} dx' \right) dk \quad (2)$$

where $Z_0(x)$ is the detrended elevation profile, $Z_0(x)$ = $Z(x)$- <$Z(x)$>; x is the horizontal location; $Z(x)$ is the bed elevation; < $Z(x)$> is the mean bed elevation of a profile of length l.

Then, the slope of the detrended bed profile, $sl(x) = \partial Z_0(x)/\partial x$, is used to obtain a frequency roughness of the second parameter η, indicating the horizontal irregularity of the bed. That is,

$$\eta = \frac{\xi_t}{\xi_{sl}} = \frac{\int_{k_1}^{k_2} S(k)dk}{\int_{k_1}^{k_2} S_{sl}(k)dk} = \frac{\int_{k_1}^{k_2} (\frac{1}{l}\int_{-\infty}^{\infty} Z_0(x)e^{-ikx}dx \int_{-\infty}^{\infty} Z_0(x')e^{-ikx'}dx')dk}{\int_{k_1}^{k_2} (\frac{1}{l}\int_{-\infty}^{\infty} \frac{dZ_0(x)}{dx}e^{-ikx}dx \int_{-\infty}^{\infty} \frac{dZ_0(x')}{dx}e^{-ikx'}dx')dk} \quad (3)$$

Finally, the total roughness (ξ_t), given that the integral is between 0 and ∞, is equal to half the mean square of the bed elevation profile with units of m^2 [25,30]. Therefore, the basal roughness indexes $\sqrt{2\xi_t}$ and $\sqrt{2\eta}$, similarly adopted by Wright et al. [30], were used to analyze the basal roughness of subglacial bed topography in a quantitative manner [30].

3. Results and Analysis

3.1. Internal Layers along the Traverse

Figure 3 shows a regional view of the IPR profile along the traverse and of the overall internal layering properties calculated using the ILCI method. The profile of the subregion has been stitched, where the breaks indicate that the profile interval is more than 5 km. The colorbar above the profile represents ILCI of the middle three-fifths of the full ice column, calculated from 500-trace moving windows (~2 km). The result of internal layering properties by ILCI can also be qualitatively seen from the radar profile.

As shown in Figure 3, areas with clear and consecutive internal layers return a high ILCI; while areas with disrupt or absent internal layers return a low ILCI. The radar profiles at 71–185 km and 267–320 km show significant quality differences. These regional data are interfered during the field acquisition, resulting in the decline of both the radar data quality and the ILCI value. Beyond that, Zone A and Zone B (except around 400 km) have middle ILCI and Zone D has relatively low ILCI, where the internal layers are discontinuous or disrupted. In particular, Zone D is located at the upstream of the Lambert Glacier region, characterized by a wide valley with deep depression at the bottom (Figure 3d), where most of the bedrock cannot be detected probably due to the scattering and absorption of radar signals. In this area, the ice thickness is greater than 3000 m and the undulation amplitude of internal layers is relatively small, indicating that the bed undulation range may be small and the base groove may be shallow. Moreover, the parallel and continuous internal layers near the surface are located above the deep disrupted layers, and most deep internal layer structures resemble "whirlwinds" or "tornados" [18], as shown in Figure 3d, which reveals the white rectangle of T area. These features of internal layers, disrupted and obliterated by the vertical to sub-vertical low reflectivity zone, are the complex response of radar signals to the high-amplitude buckling of layers within the ice sheet [48]. The structure in T, for instance, embodies the physical features of the ice sheet and is presented as "whirlwinds" in the radar profile. Thus, the whirlwind can be used to identify and map the areas with buckled and disrupted layering [17].

Except for the Zone D area, the undulation pattern of the internal layers along the traverse is similar to that of the bed topography, and the undulation amplitude of the internal layers close to the ice surface is smaller. Zone C has a median ILCI with clearly continuous internal layers distributed parallel to the bed and discontinuous or absent internal layers in the deep ice (> 1000 m depth). Zone E is the area near Dome A in the inland center of the Antarctic ice sheet, with a relatively high ILCI and significant fluctuations (Figure 3e). In Zone E, the clear internal layers extend almost to the bed, and the largest proportion of clear internal layer thickness exceeds 90% of the ice thickness. Although the age of the internal layers along the traverse is not estimated, the age-depth relationship at Kunlun Station has been derived by connecting the Vostok ice core drill site and Dome A [49]. This suggests that the ice at 48%–53% of ice thickness at Kunlun Station is 118.6–160.4 ka and the ice at 66% of ice thickness at Dome A is 160.4 ka, meaning that the deeper ice with continuous internal layers in Dome A extends well beyond the late stage of Middle Pleistocene. In local regions (such as near 735 km, 740 km,

1010 km, 1167 km, and 1208 km), the low ILCI may be the result of destructive interference caused by stacking adjacent traces with the asynchronous reflected signal at steep peaks and deep valleys [48].

3.2. Internal Layers Change with Depth

ILCI can not only represent the single result of each column by a depth detection window, but also consider the results of different depth ranges. ILCI calculated by different depth represents the characteristics of internal layers at different times and is often used to infer the history of ice flow [16]. The ice column was divided into five equal parts to calculate ILCI for specific ice depths and to average over each 500-trace window (~2 km) and each 2500-trace window (~10 km) (Figure 4). The smoothing over 500 traces is used to identify anomalies, while the smoothing over 2500 traces gives a clearer regional picture; hence, both plots are included in Figure 4. Here, 0%–20% (Figure 4a) and 80%–100% (Figure 4e) of the ice column represent its upper and lower fifths discarded in the previous analysis, respectively. As shown in Figure 4a, there are some changes in the internal layering of the upper fifth of the ice along the traverse, but it is generally affected by the poor ability of the radar to resolve layers to a certain extent, which produces a series of interference-based flat layers (equivalent to high ILCI). In Figure 4e, the signal with slight changes is degraded by the dominated background noise, which produces a significantly low ILCI. This accounts for the omission of at least a proportion of the upper and lower ice when applying the ILCI method.

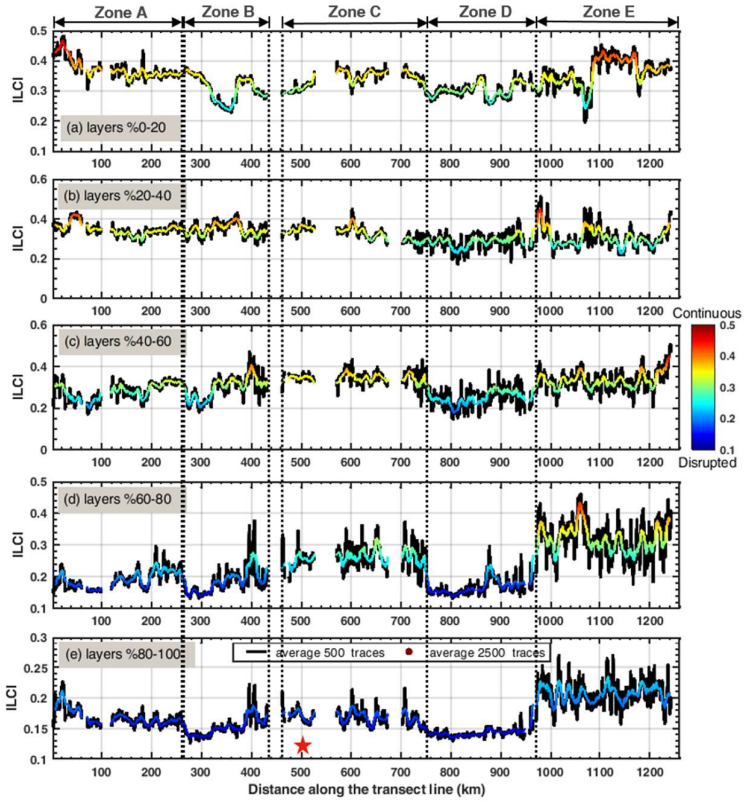

Figure 4. ILCI graph of depth range from Zhongshan to Dome A. (**a**–**e**) show the results derived progressively at the decline in each fifth of the ice. The black line indicates the result of 500-trace moving windows, and the color scatter is the result of 2500-trace moving windows. The red star marks the location of Taishan Station.

Figure 4b–d display significant changes with depth in the continuity of internal layers along the Travers. All regions, except Zone E, have a tendency to decrease with increasing depth. Notably, the region (320–750 km) has a high ILCI (>0.3) in both the shallow (20%–40%) and middle (40%–60%) areas. ILCI in some shallow areas (1000–1070 km and 1120–1220 km) is lower than that in other areas

of Zone E. Both of Zone C and Zone E have a higher ILCI than other regions at different depths. All of ILCI at different depths are low (<0.3) in Zone D. The variation of ILCI with depth may to some extent reflect the changes in the englacial conditions at different periods [16,50]. The next section will focus on the specific explanation of these areas.

3.3. Subglacial Conditions

As shown in Figure 5a, the distribution of the bed elevation reveals that there exists a variety of mountainous topography in PEL. The subglacial topography is mainly dominated by mountainous and valley glaciers. Within a range of 0–100 km near the coast, the bed undulation is relatively flat and the bed elevation is close to the sea level. At 120–390 km, the average bed elevation is 380 m with an obvious fluctuation range, while the average elevation at 390–420 km is about 1000 m with a greater undulation frequency. In addition, the bed is undulating with many deep valleys and high peaks at 420–750 km near the east upstream of Lambert Glacier. The entire bed topography in the upstream of Lambert Glacier cannot be detected due to insufficient ice-penetrating capability of IPR, and the basal roughness cannot be accurately assessed as well. It is found that no significant abrupt change of amplitude is reflected in the distribution of the internal layers, and the overall distribution is similar. Presumably, this area may have similar topographical features on the basis of the partial bed topography. Therefore, the bed topography depicted in upstream of the Lambert Glacier is supposed to be established, showing that the largest deep valley is about 165 km wide and the bed elevation may be below sea level. Due to the existence of GSM, there are deep valleys and peaks at Dome A, where the average bed elevation is above 2000 m and the variation is relatively frequently and intense. At the edge of Lambert Glacier and GSM, the relative bed elevation difference is approximately 1200 m. The difference between the average bed elevation of Zone E in the GSM region and other zones is more than 800 m. The changes in the basal thermal mechanism caused thinning of ice sheet and the subglacial topography of higher elevation have imposed a significant impact on the basal roughness [32].

Basal roughness distribution except for the area where the bed is not detected in upstream of Lambert Glacier is shown in Figure 5b. To better characterize the region, a smoothing average of 500 (2 km) and 2500 (10 km) traces was performed for the total roughness ξ_t and frequency roughness η (Figure 5b). There is a high total roughness in the regions at 390–410 km and Zone E, and a low total roughness along the traverse in other regions, while most of the frequency roughness has a relatively high value, except the regions at 220–390 km and Zone D. Here, the entire basal roughness is divided into three types (Table 2), which are: low ξ_t low η area (220–390km and Zone D), low ξ_t high η area (0–220 km and 410–750 km), and high ξ_t high η area (390–410 km and Zone E).

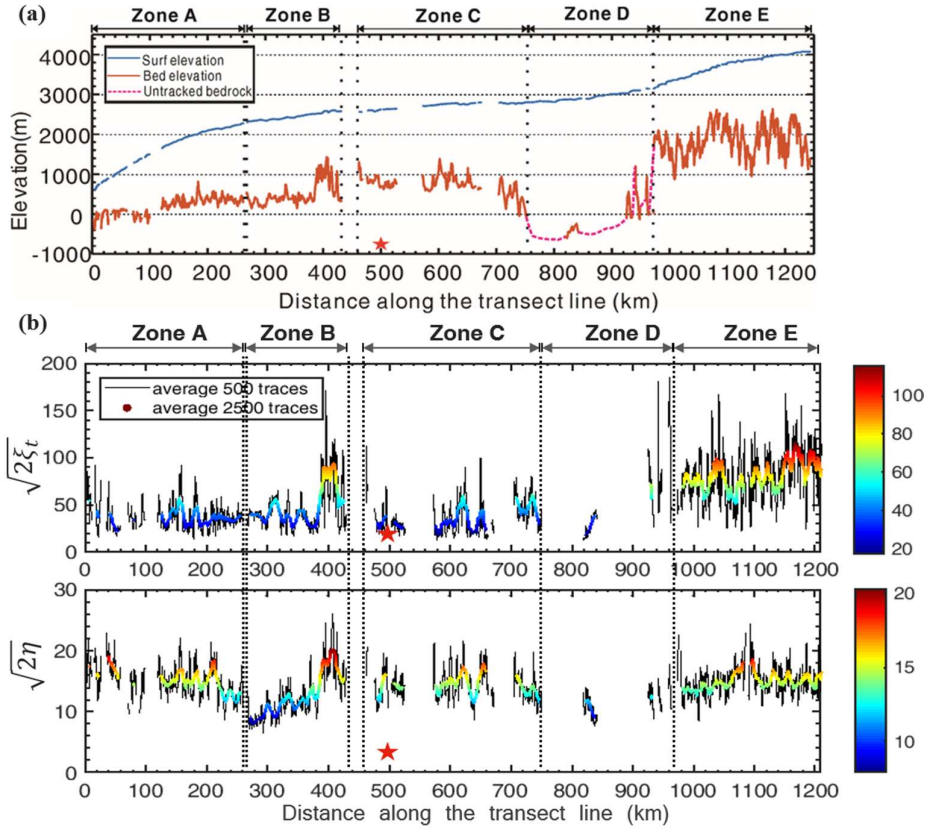

Figure 5. (**a**) Surface and bed elevation, (**b**) basal roughness from Zhongshan to Dome A. The black line indicates the result from 500-trace moving windows, and the color scatter is the result from 2500-trace moving windows. The red star marks the location of Taishan Station.

4. Discussion

IPR data reveal some subsurface features associated with ice dynamics, including the bed topography and internal layers. In general, the internal layers are deformed by the bed topography, basal conditions, accumulation and ice flow [10]. It can be seen in Figure 3 that all profiles display a pattern of folds in a distinct trough-and-crest of internal layers. The folds may be generated by numerous processes, such as the flow convergence or divergence in the ice stream tributary system, the flow over undulated bedrock, the nonuniform basal melting or surface accumulation, and the ice deflection over bed obstacle or ice deformation in response to variable basal conditions [7,10]. Except for Zone D, the distribution of internal layer folds is similar to the bed as indicated in the profiles along the traverse (Figure 3), which implies that the internal layers are probably dominated by the shape of the bedrock. Whereas for Zone D, many discontinuous and disrupted folds may be inconsistent with the bed topography. The changes in the internal layers through the upstream of Lambert Glacier may be explained by the ice flow rather than the shape of bedrock. Yet the spatiotemporal properties of such processes are uncertain and so is the origin of the folds along the traverse. The folds in the internal layers carry important original flow characteristics.

In this study, the surface ice velocity along the traverse was taken into account, which is taken from the National Snow and Ice Data Center MEaSUREs database derived by the interferometric synthetic aperture radar (InSAR) survey from 1996 to 2016 [51,52], and its verification was conducted with ground-based GPS measurements (2005–2016) given in Yang et al. [2018] [39]. Figure 6 shows that the ice radar track is basically perpendicular or oblique to the ice flow. However, only if the radar track parallels ice flow (in very few cases) would the ILCI method fail to identify disruption to layers; and the ILCI of internal layering disruption will be similar from any other angle between the direction of

radar track and ice flow [16]. Therefore, the influence of the ice flow direction on the internal layering will be not discussed in this paper.

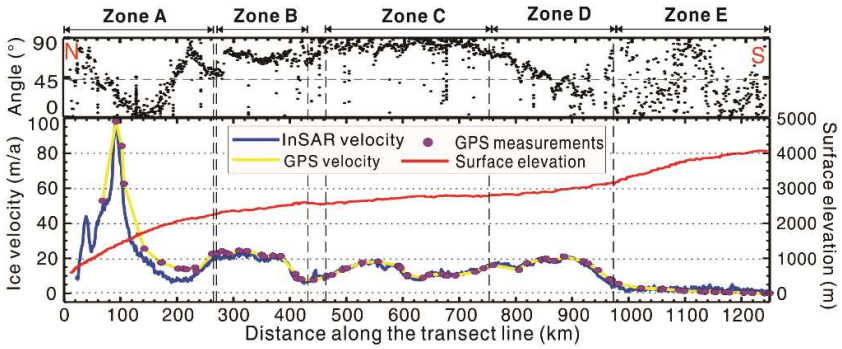

Figure 6. Surface elevation (red line), surface ice velocity distribution along the Chinese National Antarctic Research Expedition (CHINARE) traverse, and the angles between ice-flow and the traverse (black dot). The surface ice velocity vectors are derived from interferometric synthetic aperture radar (InSAR) data (blue line) [51,52] and Global Positioning System (GPS) data (yellow line) [39]. The purple points stand for the position of GPS measurement points. The red star marks the location of Taishan Station.

ILCI in combination with depth can not only assess the relative changes in the continuity of internal layers but also provide insight into the history of ice flow [16,50]. The ILCI in the 0–390 km and Zone D regions (Figure 4b–d) gradually decreases with increasing depth, which does not match the current slow ice velocity (< 100 m a^{-1}, Figure 6). The low ILCI of the disrupted layer in Zone D and the current slow surface ice velocity (< 20 m a^{-1}) may provide evidence for the existence of previous faster or enhanced flow, indicating a stagnant period of the ice stream [16,17]. Both of the shallow and middle layers (20%–60%) in the 390–750 km areas and Zone E have relatively high ILCI, indicating the influence of undulating mountainous terrain. Here, the height of the terrain is able to limit the ice flow, and all of the internal layers maintain the spatial structure. The low ILCI of other layers may be associated with changes in bed conditions and ice fabrics [16,32,34]. The internal layers in some areas of GSM are discontinuous because of recent or former megadunes and surface erosion by wind erosion or sublimation [5,53,54]. This may be the reason for the relatively low ILCI of the shallow layers in Zone E.

The variation in the internal layers and bed topography observed by IPR data can be used to reveal the fast or enhanced flow regions in which satellite-derived ice velocity is not available. Basal roughness plays an important role in elucidating basal conditions and the possible history of ice dynamics history [9]. Indeed, the principal factors affecting basal roughness include not only ice dynamics, but also marine/continental setting, preglacial topography/geological structure, basal thermal regime, and subglacial erosion/deposition, many of which are interrelated. For example, the smooth bed with low roughness may be due to high erosion/deposition rate associated with fast ice flow (> 100 m a^{-1}) and warm basal ice of marine setting; while the rough bed with high roughness is likely due to slow ice flow associated with low erosion/deposition and cold basal ice of continental setting [9,27,29]. However, it is likely that a continental setting intensively eroded by fast ice flow has a similar value of roughness (ξ_t) to a high deposition rate of marine setting [25]. In order to more precisely describe and distinguish between subglacial process domains, Li used a two-parameter index, $\{\xi_t, \eta\}$, to provide a reference [25]. There are three types of basal roughness along the traverse (Figure 5, Figure 7). The first basal roughness characteristics type of low ξ_t low η indicates that the relatively smooth bed topography may be eroded by the ancient fast ice flow. This is consistent with the result of internal layers being discontinuous with the increasing depth, further providing evidence for the existence of previous rapid ice flow (Figure 7). The second basal roughness type of low ξ_t high η concludes the 0–220 km region with low ILCI and Zone C with relatively high ILCI. Low ξ_t represents

small amplitude of bed topography fluctuations, which may be caused by erosion; high η implies that the long-wavelength roughness region may have experienced deposition [25,26,30]. Here, the region of 0–220 km is preliminarily considered a product of fast flow erosion and sediment-filling of valleys [25], and the region of Zone C is likely to be dominated by deposition. The third basal roughness type of high ξ_t high η presents that typical mountainous upland landscapes are found in the regions (390–410km and Zone E). There is a cold basal thermal state (about –20 °C at Dome A), which is largely unaffected by the current slow ice flow (ice flow rate < 5 m a^{-1}) of continental setting [25,27,30].

It is worth noting that the ILCI and basal roughness as interpretative tools can quantify the characteristics of the internal layer and bed topography. However, the available data with only one radar profile are not enough to interpret the ice dynamics, which requires a wide range of ice radar data and remote sensing data to provide further explanation.

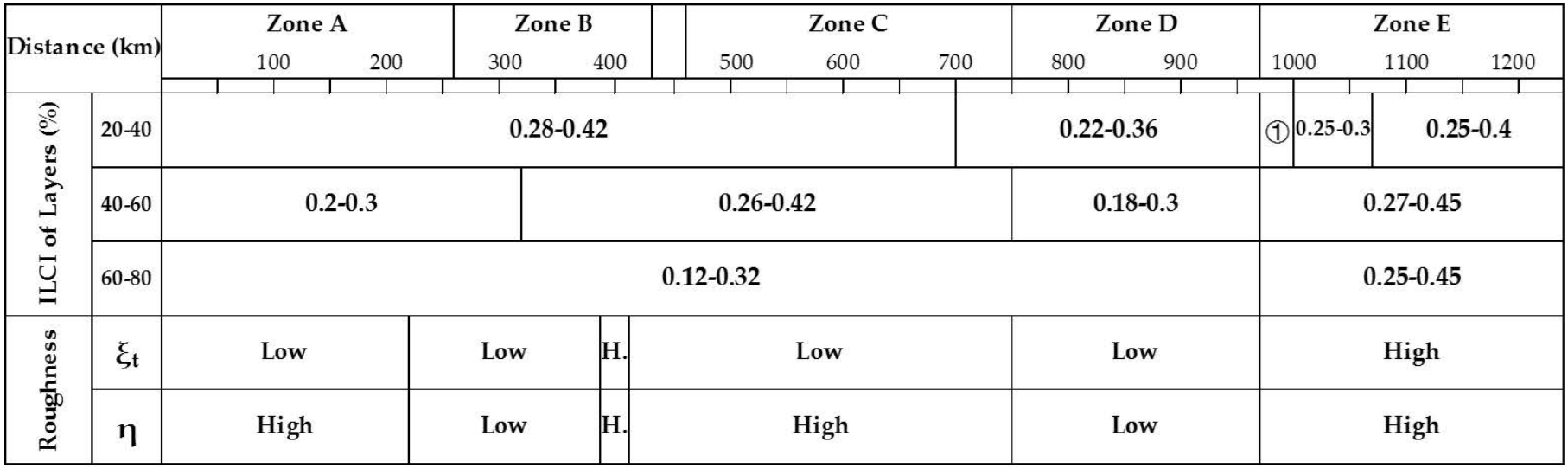

Figure 7. Distribution of Internal Layering Continuity Index (ILCI) with depth and three types of the basal roughness along the traverse from Zhongshan to Dome A.

5. Conclusions

IPR data along the traverse between Zhongshan Station and Dome A of EAIS were used to detailedly analyze the internal stratigraphy and basal roughness in the PEL. Large numbers of internal layer folds in all the regions, except for the upstream of Lambert Glacier, are dominated by the bed topography. The results find that ILCI decreases with increasing depth, and that there are three types of basal roughness in the region of 0–430 km (Zone A and Zone B). The ILCI is medium in the region of 460–750 km (Zone C), where the internal layers are distributed parallel to the bed with low amplitude and long wavelength. The buckled and disrupted internal layers in the upstream of Lambert Glacier (Zone D) indicate that there may have been a rapid or enhanced ice flow previously. Dome A (Zone E) has clear internal layers with high ILCI, and the ratio of the continuous and visible layer thickness is more than 90%, indicating that it has prevailed throughout at least the late stage of Middle Pleistocene, and the rough bed topography is largely unaffected by slow ice flow.

There are many uncertainties in the results due to the limitation of a single radar route in this paper, such as ice flow direction, basal conditions, and surface accumulation, and the understanding of the internal structural properties and the basal roughness is not yet complete. However, the results provide not only an opportunity for the discussion of internal mechanisms and ice flow history in PEL of EAIS, but also a data foundation for ice sheet modeling and age calculations. In future research, airborne IPR data may cover this route as well as the entire PEL. This paper provides a wide range of basal roughness and ice flow history of EAIS by comparison for further discussion. In the future, higher-dimension geophysical observations and modeling will be further selected to help explain the ice dynamics of the PEL, East Antarctica.

Author Contributions: Conceptualization, S.L. and X.T.; methodology, K.L.; software, K.L.; S.L.; and T.W.; validation, K.L.; S.L.; and X.T.; formal analysis, K.L.; investigation, J.G.; L.L.; and X.C.; resources, X.T.; J.G.; L.L.; and B.S.; data curation, X.T.; writing—original draft preparation, K.L.; writing—review and editing, K.L.; S.L.; and X.T.; supervision, S.L.; X.T.; and B.S. All authors have read and agreed to the published version of the manuscript.

Funding: This study is supported by the National Natural Science Foundation of China (Nos. 41876230, 41876227, 41776186, 41730102, 41941006) and the Chinese Polar Environmental Comprehensive Investigation and Assessment Programs (CHINARE 2017-02-02).

Acknowledgments: The authors thank the Chinese National Antarctic Research Expedition for their help in the field data collection.

Conflicts of Interest: The authors declare no conflict of interest.

References

1. AitkeniD, A.R.; Roberts, J.L.; Van Ommen, T.; Young, D.A.; Golledge, N.; Greenbaum, J.S.; Blankenship, D.D.; Siegert, M.J. Repeated large-scale retreat and advance of Totten Glacier indicated by inland bed erosion. *Nature* **2016**, *533*, 385–389. [CrossRef] [PubMed]
2. Gulick, S.P.S.; Shevenell, A.E.; Montelli, A.; Fernandez, R.; Smith, C.; Warny, S.; Bohaty, S.M.; Sjunneskog, C.; Leventer, A.; Frederick, B.; et al. Initiation and long-term instability of the East Antarctic Ice Sheet. *Nature* **2017**, *552*, 225–229. [CrossRef] [PubMed]
3. Sime, L.C.; Karlsson, N.B.; Paden, J.D.; Gogineni, S. Isochronous information in a Greenland ice sheet radio echo sounding data set. *Geophys. Res. Lett.* **2014**, *41*, 1593–1599. [CrossRef]
4. Wang, B.; Sun, B.; Martín, C.; Ferraccioli, F.; Steinhage, D.; Cui, X.; Siegert, M.J. Summit of the East Antarctic Ice Sheet underlain by thick ice-crystal fabric layers linked to glacial–interglacial environmental change. *Geol. Soc.* **2017**, *461*, 131–143. [CrossRef]
5. Winter, A.; Steinhage, D.; Creyts, T.T.; Kleiner, T.; Eisen, O. Age stratigraphy in the East Antarctic Ice Sheet inferred from radio-echo sounding horizons. *Earth Syst. Sci. Data* **2019**, *11*, 1069–1081. [CrossRef]
6. Rippin, D.; Siegert, M.; Bamber, J. The englacial stratigraphy of Wilkes Land, East Antarctica, as revealed by internal radio-echo sounding layering, and its relationship with balance velocities. *Ann. Glaciol.* **2003**, *36*, 189–196. [CrossRef]

7. Ng, F.S.L.; Conway, H. Fast-flow signature in the stagnated Kamb Ice Stream, West Antarctica. *Geology* **2004**, *32*, 481–484, ISSN 0091-7613. [CrossRef]
8. Bingham, R.G.; Siegert, M.; Young, D.; Blankenship, D.D. Organized flow from the South Pole to the Filchner-Ronne ice shelf: An assessment of balance velocities in interior East Antarctica using radio echo sounding data. *J. Geophys. Res. Space Phys.* **2007**, *112*, F03S26. [CrossRef]
9. Bingham, R.G.; Siegert, M. Quantifying subglacial bed roughness in Antarctica: Implications for ice-sheet dynamics and history. *Quat. Sci. Rev.* **2009**, *28*, 223–236. [CrossRef]
10. Keisling, B.A.; Christianson, K.; Alley, R.B.; Peters, L.E.; Christian, J.E.; Anandakrishnan, S.; Riverman, K.L.; Muto, A.; Jacobel, R.W. Basal conditions and ice dynamics inferred from radar-derived internal stratigraphy of the northeast Greenland ice stream. *Ann. Glaciol.* **2014**, *55*, 127–137. [CrossRef]
11. Wilkens, N.; Behrens, J.; Kleiner, T.; Rippin, D.; Rückamp, M.; Humbert, A. Thermal structure and basal sliding parametrisation at Pine Island Glacier—A 3-D full-Stokes model study. *Cryosphere* **2015**, *9*, 675–690. [CrossRef]
12. Fahnestock, M.; Abdalati, W.; Joughin, I.; Brozena, J.; Gogineni, P. High Geothermal Heat Flow, Basal Melt, and the Origin of Rapid Ice Flow in Central Greenland. *Science* **2001**, *294*, 2338–2342. [CrossRef] [PubMed]
13. Fischer, H.; Severinghaus, J.; Brook, E.; Wolff, E.; Albert, M.; Alemany, O.; Arthern, R.; Bentley, C.; Blankenship, D.; Chappellaz, J.; et al. Where to find 1.5 million yr old ice for the IPICS "Oldest-Ice" ice core. *Clim. Past* **2013**, *9*, 2489–2505. [CrossRef]
14. Young, D.; Roberts, J.L.; Ritz, C.; Frezzotti, M.; Quartini, E.; Cavitte, M.; Tozer, C.R.; Steinhage, D.; Urbini, S.; Corr, H.F.J.; et al. High-resolution boundary conditions of an old ice target near Dome C, Antarctica. *Cryosphere* **2017**, *11*, 1897–1911. [CrossRef]
15. Cui, X.; Sun, B.; Tian, G.; Jiang, Y.; Zhang, X.; Guo, J.; Tang, X. Progress and prospect of ice radar in investigating and researching Antarctic ice sheet. *Adv. Earth Sci.* **2009**, *24*, 392–402.
16. Bingham, R.G.; Rippin, D.; Karlsson, N.B.; Ferraccioli, F.; Jordan, T.A.; Le Brocq, A.M.; Rose, K.C.; Ross, N.; Siegert, M.; Corr, H.F. Ice-flow structure and ice dynamic changes in the Weddell Sea sector of West Antarctica from radar-imaged internal layering. *J. Geophys. Res. Earth Surf.* **2015**, *120*, 655–670. [CrossRef]
17. Winter, K.; Woodward, J.; Ross, N.; Dunning, S.; Bingham, R.G.; Corr, H.F.J.; Siegert, M. Airborne radar evidence for tributary flow switching in Institute Ice Stream, West Antarctica: Implications for ice sheet configuration and dynamics. *J. Geophys. Res. Earth Surf.* **2015**, *120*, 1611–1625. [CrossRef]
18. Karlsson, N.B.; Rippin, D.M.; Vaughan, D.; Corr, H.F. The internal layering of Pine Island Glacier, West Antarctica, from airborne radar-sounding data. *Ann. Glaciol.* **2009**, *50*, 141–146. [CrossRef]
19. Karlsson, N.B.; Rippin, D.M.; Bingham, R.G.; Vaughan, D. A 'continuity-index' for assessing ice-sheet dynamics from radar-sounded internal layers. *Earth Planet. Sci. Lett.* **2012**, *335*, 88–94. [CrossRef]
20. Holt, J.W.; Blankenship, D.D.; Morse, D.L.; Young, D.; Peters, M.E.; Kempf, S.D.; Richter, T.G.; Vaughan, D.; Corr, H.F.J. New boundary conditions for the West Antarctic Ice Sheet: Subglacial topography of the Thwaites and Smith glacier catchments. *Geophys. Res. Lett.* **2006**, *33*, 72–88. [CrossRef]
21. Bingham, R.G.; Siegert, M. Radar-derived bed roughness characterization of Institute and Möller ice streams, West Antarctica, and comparison with Siple Coast ice streams. *Geophys. Res. Lett.* **2007**, *34*, L21504. [CrossRef]
22. Siegert, M.J.; Le Brocq, A.; Payne, A.J. Hydrological Connections between Antarctic Subglacial Lakes, the Flow of Water beneath the East Antarctic Ice Sheet and Implications for Sedimentary Processes. *Glacial Sediment. Process. Prod.* **2009**, *39*, 3–10.
23. Pattyn, F. Antarctic subglacial conditions inferred from a hybrid ice sheet/ice stream model. *Earth Planet. Sci. Lett.* **2010**, *295*, 451–461. [CrossRef]
24. Bell, R.E.; Ferraccioli, F.; Creyts, T.T.; Braaten, D.; Corr, H.; Das, I.; Damaske, D.; Frearson, N.; Jordan, T.A.; Rose, K.; et al. Widespread Persistent Thickening of the East Antarctic Ice Sheet by Freezing from the Base. *Science* **2011**, *331*, 1592–1595. [CrossRef] [PubMed]
25. Li, X.; Sun, B.; Siegert, M.; Bingham, R.G.; Tang, X.; Zhang, N.; Cui, X.; Zhang, X. Characterization of subglacial landscapes by a two-parameter roughness index. *J. Glaciol.* **2010**, *56*, 831–836. [CrossRef]
26. Rippin, D.M.; Bingham, R.G.; Jordan, T.A.; Wright, A.; Ross, N.; Corr, H.; Ferraccioli, F.; Le Brocq, A.; Rose, K.; Siegert, M. Basal roughness of the Institute and Möller Ice Streams, West Antarctica: Process determination and landscape interpretation. *Geomorphology* **2014**, *214*, 139–147. [CrossRef]
27. Siegert, M.; Taylor, J.; Payne, A.J. Spectral roughness of subglacial topography and implications for former ice-sheet dynamics in East Antarctica. *Glob. Planet. Chang.* **2005**, *45*, 249–263. [CrossRef]

28. Jordan, T.; Cooper, M.; Schroeder, D.; Williams, C.; Paden, J.D.; Siegert, M.; Bamber, J. Self-affine subglacial roughness: Consequences for radar scattering and basal water discrimination in northern Greenland. *Cryosphere* **2017**, *11*, 1247–1264. [CrossRef]
29. Rippin, D.; Vaughan, D.; Corr, H. The basal roughness of Pine Island Glacier, West Antarctica. *J. Glaciol.* **2011**, *57*, 67–76. [CrossRef]
30. Wright, A.P.; Young, D.; Roberts, J.L.; Schroeder, D.; Bamber, J.; Dowdeswell, J.; Young, N.W.; Le Brocq, A.; Warner, R.; Payne, A.J.; et al. Evidence of a hydrological connection between the ice divide and ice sheet margin in the Aurora Subglacial Basin, East Antarctica. *J. Geophys. Res.* **2012**, *117*, F01033. [CrossRef]
31. Fujita, S.; Holmlund, P.; Matsuoka, K.; Enomoto, H.; Fukui, K.; Nakazawa, F.; Sugiyama, S.; Surdyk, S. Radar diagnosis of the subglacial conditions in Dronning Maud Land, East Antarctica. *Cryosphere* **2012**, *6*, 1203–1219. [CrossRef]
32. Cui, X.; Sun, B.; Tian, G.; Tang, X.; Zhang, X.; Jiang, Y.; Guo, J.; Li, X. Preliminary results of ice radar investigation along the traverse between Zhongshan and Dome A in East Antarctic ice sheet: Ice thickness and subglacial topography. *Chin. Sci. Bull.* **2010**, *55*, 2715–2722. [CrossRef]
33. Cui, X.; Wang, T.; Sun, B.; Tang, X.; Guo, J. Chinese radioglaciological studies on the Antarctic ice sheet: Progress and prospects. *Adv. Polar Sci.* **2017**, *28*, 161–170. [CrossRef]
34. Tang, X.; Sun, B.; Guo, J.; Liu, X.; Cui, X.; Zhao, B.; Chen, Y. A freeze-on ice zone along the Zhongshan–Kunlun ice sheet profile, East Antarctica, by a new ground-based ice-penetrating radar. *Sci. Bull.* **2015**, *60*, 574–576. [CrossRef]
35. Tang, X.; Guo, J.; Sun, B.; Wang, T.; Cui, X. Ice thickness, internal layers, and surface and subglacial topography in the vicinity of Chinese Antarctic Taishan station in Princess Elizabeth Land, East Antarctica. *Appl. Geophys.* **2016**, *13*, 203–208. [CrossRef]
36. Ding, M.; Xiao, C.; Li, Y.; Ren, J.; Hou, S.; Jin, B.; Sun, B. Spatial variability of surface mass balance along a traverse route from Zhongshan station to Dome A, Antarctica. *J. Glaciol.* **2011**, *57*, 658–666.
37. Ding, M.; Xiao, C.; Li, C.; Qin, D.; Jin, B.; Shi, G.; Xie, A.; Cui, X. Surface mass balance and its climate significance from the coast to Dome A, East Antarctica. *Sci. China Earth Sci.* **2015**, *58*, 1787–1797. [CrossRef]
38. Zhang, S.E.D.; Wang, Z.; Li, Y.; Jin, B.; Zhou, C. Ice velocity from static GPS observations along the transect from Zhongshan station to Dome A, East Antarctica. *Ann. Glaciol.* **2008**, *48*, 113–118.
39. Yang, Y.; Ke, H.; Wang, Z.; Li, F.; Ding, M.; Sun, B.; Jin, B.; Wang, L.; Ai, S. Decadal GPS-derived ice surface velocity along the transect from Zhongshan Station to and around Dome Argus, East Antarctica, 2005–2016. *Ann. Glaciol.* **2018**, *59*, 1–9.
40. Fretwell, P.; Pritchard, H.D.; Vaughan, D.; Bamber, J.; Barrand, N.E.; Bell, R.; Bianchi, C.; Bingham, R.G.; Blankenship, D.D.; Casassa, G.; et al. Bedmap2: Improved ice bed, surface and thickness datasets for Antarctica. *Cryosphere* **2013**, *7*, 375–393. [CrossRef]
41. Greene, C.A.; Gwyther, D.; Blankenship, D.D. Antarctic Mapping Tools for Matlab. *Comput. Geosci.* **2017**, *104*, 151–157. [CrossRef]
42. Cumming, I.G.; Wong, F.H. *Digital Processing of Synthetic Aperture Radar Data: Algorithms and Implementation*; Artech House: Boston, MA, USA, 2005.
43. Liu, X.; Lang, S.; Zhao, B.; Zhang, F.; Liu, Q.; Tang, C.; Li, D.; Fang, G. High-Resolution Ice-Sounding Radar Measurements of Ice Thickness Over East Antarctic Ice Sheet as a Part of Chinese National Antarctic Research Expedition. *IEEE Trans. Geosci. Remote. Sens.* **2018**, *56*, 3657–3666. [CrossRef]
44. Gupta, G. Algorithm for image processing using improved median filter and comparison of mean, median and improved median filter. *Int. J. Soft Comput. Eng. (IJSCE)* **2011**, *1*, 304–311.
45. Steinhage, D.; Nixdorf, U.; Meyer, U.; Miller, H. Subglacial topography and internal structure of central and western Dronning Maud Land, Antarctica, determined from airborne radio echo sounding. *J. Appl. Geophys.* **2001**, *47*, 183–189. [CrossRef]
46. Karlsson, N.B.; Binder, T.; Eagles, G.; Helm, V.; Pattyn, F.; Van Liefferinge, B.; Eisen, O. Glaciological characteristics in the Dome Fuji region and new assessment for "Oldest Ice". *Cryosphere* **2018**, *12*, 2413–2424. [CrossRef]
47. Taylor, J.; Siegert, M.; Payne, A.J.; Hubbard, B. Regional-scale bed roughness beneath ice masses: Measurement and analysis. *Comput. Geosci.* **2004**, *30*, 899–908. [CrossRef]
48. Holschuh, N.; Christianson, K.; Anandakrishnan, S. Power loss in dipping internal reflectors, imaged using ice-penetrating radar. *Ann. Glaciol.* **2014**, *55*, 49–56. [CrossRef]

49. Tang, X.-Y.; Sun, B.; Wang, T. Radar isochronic layer dating for a deep ice core at Kunlun Station, Antarctica. *Sci. China Earth Sci.* **2019**, *63*, 303–308. [CrossRef]
50. Winter, K.; Woodward, J.; Dunning, S.; Turney, C.; Fogwill, C.J.; Hein, A.S.; Golledge, N.; Bingham, R.G.; Marrero, S.; Sugden, D.E.; et al. Assessing the continuity of the blue ice climate record at Patriot Hills, Horseshoe Valley, West Antarctica. *Geophys. Res. Lett.* **2016**, *43*, 2019–2026. [CrossRef]
51. Rignot, E.; Mouginot, J.; Scheuchl, B. Ice Flow of the Antarctic Ice Sheet. *Science* **2011**, *333*, 1427–1430. [CrossRef]
52. Rignot, E.; Mouginot, J.; Scheuchl, B. *MEaSUREs InSAR-Based Antarctica Ice Velocity Map, Version 2. [Indicate Subset Used*; NASA National Snow and Ice Data Center Distributed Active Archive Center: Boulder, CO, USA.
53. Das, I.; Bell, R.E.; Scambos, T.A.; Wolovick, M.; Creyts, T.T.; Studinger, M.; Frearson, N.; Nicolas, J.P.; Lenaerts, J.; Broeke, M.V.D. Influence of persistent wind scour on the surface mass balance of Antarctica. *Nat. Geosci.* **2013**, *6*, 367–371. [CrossRef]
54. Scambos, T.; Frezzotti, M.; Haran, T.; Bohlander, J.; Lenaerts, J.; Broeke, M.V.D.; Jezek, K.; Long, D.G.; Urbini, S.; Farness, K.; et al. Extent of low-accumulation 'wind glaze' areas on the East Antarctic plateau: Implications for continental ice mass balance. *J. Glaciol.* **2012**, *58*, 633–647. [CrossRef]